Energy Advances

ROYAL SOCIETY OF CHEMISTRY

COMMUNICATION

View Article Online
View Journal | View Issue

Cite this: *Energy Adv.*, 2023, 2, 797

Received 12th April 2023,
Accepted 22nd May 2023

DOI: 10.1039/d3ya00158j

rsc.li/energy-advances

An aqueous rechargeable and high-capacity zinc ion battery using a novel rGO–V_2O_5–SiO_2 hybrid nanocomposite as a cathode material†

Akash Lata, [a] Anuj Kumar,[a] Gautam Biswas,[b] Nripen Chanda [c] and Ravi Kumar Arun *[a]

We report an aqueous Zn–rGO–V_2O_5–SiO_2 pouch-type rechargeable zinc ion battery (ZIB) with a rGO–V_2O_5–SiO_2 hybrid nanocomposite as the cathode, Zn as the anode, and 0.5 M Zn $(CF_3SO_3)_2$ as the electrolyte. The rGO–V_2O_5–SiO_2 hybrid cathode, in the presence of an aqueous electrolyte, intercalated Zn^{2+} ions in its 3D layers due to the high surface area and porosity of the developed nanorod structures. Furthermore, the combined electrical conductivity of rGO and V_2O_5 with high water adsorption capacity of silica synergistically affects the charge–discharge rate and stability of the ZIB. As a result, the aqueous rechargeable battery depicts a specific charge capacity of 640 mA h g^{-1} at 200 mA g^{-1} and a high-performance rate of 890 mA h g^{-1} at 20 mA g^{-1} which are further stacked in series to obtain a capacity of 502 mA h g^{-1} at 12 V. The pouch cell configuration makes this battery a potential candidate for large-scale energy storage applications.

1. Introduction

In today's era, while energy demand is continuously increasing, the quest for alternative energy sources is on the rise.[1–3] The electrochemical energy storage devices, such as batteries and fuel cells, that can integrate with the renewable energy systems can fill this deficit and provide a clean energy solution.[4,5] Currently, the largest market share of portable electronics belongs to lithium-ion batteries, and they are widely applicable due to their long-life cycles, high energy densities and wider working voltage range.[6,7] However, their prolonged usage is hindered by the limited resources of Li, its high cost, and the combustible organic electrolytes.[8] Comparatively, aqueous rechargeable batteries are a promising candidate with naturally abundant Na^+, K^+, and Zn^{2+} ions.[9] Among them, exceptional properties have been shown by the aqueous rechargeable Zinc ion batteries (ZIBs) with a high volumetric capacity and low redox potential of Zn/Zn^{2+} (−0.762 V *vs.* SHE).[10] The ZIBs have drawn extensive attention due to their low maintenance, high safety, cost effectiveness and less environmental impact.[11] However, there is still an issue with the active electrostatic synergy between $Zn^{2+}$and the positive cathode material due to the high hydrated ionic radius of Zn^{2+} (4.04–4.30 [Å]) that creates a slowdown in exchange for Zn^{2+} intercalation into the host cathode material.[12] Several efforts have been invested in developing host materials for ZIB cathodes, such as organic compounds, molybdenum-based sulfides, Prussian blue analogues (PBAs), manganese oxide, and vanadium-based oxides.[13–21] In the midst of these, vanadium pentoxide (V_2O_5) is a broadly suitable cathode material because of the high storage capacity of Zn^{2+} ions in the layered structures (~589 mA h g^{-1}).[4] However, surprisingly, crystalline V_2O_5 suffers from sluggish dispersion of divalent Zn^{2+} to augment the effective interaction along with the matrix due to unwanted structural strength in the cyclic Zn^{2+} insertion/extraction mechanism.[22] There are several ways to resolve these complications, such as pre-intercalation of V_2O_5 crystals by external molecules (*e.g.*, polymers and H_2O) and metal ions (*e.g.*, Li^+, Ca^{2+}, and Zn^{2+}), and creating additional O_2 vacancies in the V_2O_5 lattice. In this context, an amorphous V_2O_5 xerogel ($V_2O_5{\cdot}nH_2O$) has been used to overcome the sluggish reaction kinetics of Zn^{2+} to make this energy storage system fast and reversible.[23]

Amorphous V_2O_5 with a disordered structure provides a significant enhancement in the intercalation of Zn^{2+} ions with the increment of active sites and short-range diffusive paths, making it facile enough at the time of cycling of ions in comparison to crystalline V_2O_5.[24] Though amorphous V_2O_5 shows enhanced Zn^{2+} intercalation, low electrical conductivity

[a] *Department of Chemical Engineering, Indian Institute of Technology Jammu, Jammu, Jammu and Kashmir, 181221, India. E-mail: ravi.arun@iitjammu.ac.in*
[b] *Department of Mechanical Engineering, Indian Institute of Technology Kanpur, Kanpur, India*
[c] *Materials Processing and Microsystems Laboratory, CSIR-Central Mechanical Engineering Research Institute, Mahatma Gandhi Road, City Center, Durgapur 713209, West Bengal, India*

† Electronic supplementary information (ESI) available. See DOI: https://doi.org/10.1039/d3ya00158j

remains an open challenge for both crystalline V_2O_5 and amorphous V_2O_5.[25] Previously, the electrodes in ZIBs have used conductive additives such as graphene, carbon black, carbon nanotubes (CNTs), *etc.* to improve their performance.[26] Out of these, flexible 2D graphene is distinctly favorable in the creation of connected conductive networks,[27] offering effective charge transmission over the V_2O_5-based electrodes.[28] Moreover, V_2O_5 nanosheets and graphene can be coupled together, creating a vigorous 2D heterostructure that includes numerous interfacial cooperation among the two systems, and hence approaching an evident improvement in the electrical conductivity, adsorption of the metal ions, and consequent enhancement of the electrochemical performance.[29]

In addition, earlier works utilized a multistep process to synthesize V_2O_5-graphene composite electrodes, which included hydrothermal reactions, long-run sol–gel reactions, sluggish freeze-drying, and thermal post-treatments (to retain conductivity of GO).[30,31] The excessive annealing ($\geq$400 °C), however, may cause the loss of water of crystallization in V_2O_5 and deteriorate the electrochemical performance in ZIBs.[24,30] Thus, the fabrication of electrode materials requires significantly lower temperatures (150 to $\approx$200 °C) and involves GO, which is directly synthesized from the modified hummers method.[24] Regarding the structural properties of the electrode materials, the 3D structure of the anode materials has been attributed to the uniform nucleation of Zn and suppressed the dendrite growth on the anode side in a ZIB.[32] 3D SiO_2 affects the specific capacity values of the battery due to enhanced ionic diffusion owing to its excellent stability, high surface area, porous nature, and water adsorption ability.[32] The recent advancements of 3D Zn ion batteries, which have potential applications in wearable electronics, show a capacity retention of more than 84% after 1000 cycles with a capacity of 148.3 mA h g^{-1}.[33] However, unlike anode materials, no such cathode materials have the appropriate lattice structure to accommodate Zn^{2+} at high current density. Therefore, developing newer cathode material is essential to provide reversible and prompt Zn^{2+} ion intercalation/de-intercalation for better ZIB performance.

Herein, we report an aqueous rechargeable battery using a zinc anode and rGO–V_2O_5–SiO_2 hybrid composite as the cathode material to enhance the overall electrochemical performance. The rGO–V_2O_5–SiO_2 has a nanospheric 3D layer structure composed of cylindrical nanorod particles synthesized by the hydrothermal technique. The hybrid nature facilitates the insertion/extraction of Zn^{2+} during the cycling process due to the high surface area and porosity of the cathode material, thus increasing the energy storage capacity of the battery. The combined electrical conductivity of rGO and V_2O_5 with the high water adsorption capacity of silica can synergistically affect the performance rate capability and stability of the ZIB.[34,35] When used as the cathode material in aqueous rechargeable ZIBs, the rGO–V_2O_5–SiO_2 composite demonstrates a specific capacity of 640 mA h g^{-1} at 0.200 mA g^{-1} and high-performance rate of 890 mA h g^{-1} at 20 mA g^{-1}. The series combination of ZIB-based pouch cells for a 12 V stack shows the stable charge–discharge performance at 200 mA g^{-1} after 80 cycles, measured at the capacity of 502 mA h g^{-1}. The pouch cell configuration with an active material loading of $\sim$ 7.3 mg cm^{-2} is an attempt towards large scale energy application of ZIBs.

2. Results and discussion

V_2O_5 shows an orthorhombic crystal structure with short interlayer spacing.[36] To enhance the spacing between the layers, reduced graphene oxide (rGO) has been introduced between the V_2O_5 layers. Initially, SiO_2 with water absorption capacity is added to the V_2O_5. Afterward, the graphene oxide is mixed with the V_2O_5 and SiO_2, followed by a hydrothermal process which leads to redox reactions in acidic conditions. The rGO layers intercalate around the inner layers of the V_2O_5 crystal structure. This is followed by covering with the SiO_2 layer like an envelope around the V_2O_5 layers, creating cylindrical nanorods. This way, a noticeable expansion is obtained in the interlayer spacing of V_2O_5. Concurrently, the insertion of the rGO causes the limited reduction of V^{5+} to V^{4+}.[37] The mixed V_2O_5–SiO_2 and the conducting surface of rGO collectively improve the ion/electron transport kinetics of V_2O_5 leading to an efficient ion transport capacity.[37] Herein, a pouch cell configuration of Zn/rGO–V_2O_5–SiO_2 is developed *via* hydrothermal growth and by following the subsequent steps. We used carbon-coated aluminum foil as current collector, Zn foil as anode and rGO–V_2O_5–SiO_2 hybrid nanocomposite as the cathode. A packaging bag of aluminum was used with the addition of electrolyte to pack the cell. An operational exchange of ions in the cages of the cathode material is shown in Fig. 1, which depicts the intercalation-deintercalation process in the pouch cell.

The primary interactions in the cell are between the zinc ions in the electrolyte and the cathode materials. During the discharge process, the anodic Zn is oxidized to Zn^{2+} ions, which intercalate into the layered structure of rGO–V_2O_5–SiO_2. The intercalation of Zn ions into the cathode material leads to the generation of electrons, which flow through the external circuit and power the device. During the charge process, the Zn^{2+} ions reduce back to the Zn anode, and the intercalated Zn^{2+} ions

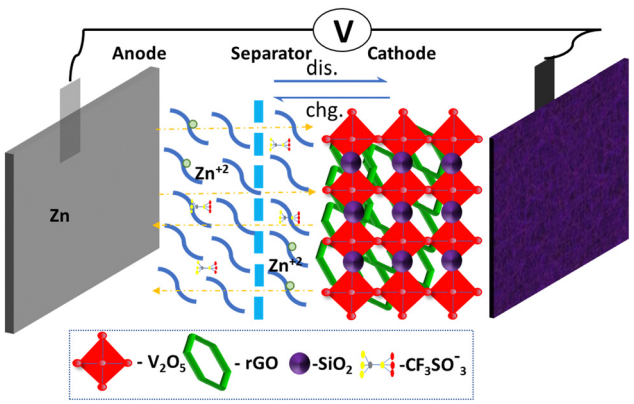

Fig. 1 Charge–discharge process with the structural alignment of the pouch cell describing the transportation of Zn^{2+} ions in the presence of electrolyte with the cathode material.

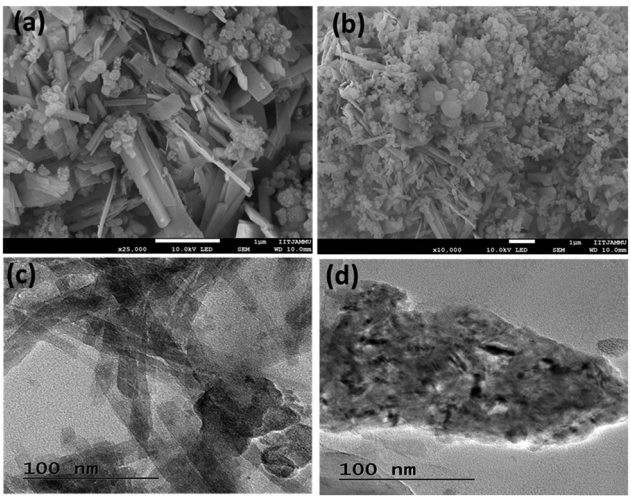

Fig. 2 (a) FESEM image of rGO–V_2O_5–SiO_2; (b) TEM image of rGO–V_2O_5–SiO_2; (c) TEM image of the composite showing square plated nanorods of V_2O_5, along with the V_2O_5–SiO_2 framework; (d) the composite of rGO–V_2O_5–SiO_2.

diffuse back to the electrolyte to keep the concentration of zinc ions constant in the electrolyte. The rGO serves as a conductive surface that improves the electrical conductivity of the cathode material. This enables faster electron transfer during the redox reactions, leading to improved battery performance.[38] Fig. 2 displays the surface morphology of the nanocomposite rGO–V_2O_5–SiO_2. As seen in Fig. 2a, the SiO_2 has a loose cotton-like structure, while the V_2O_5 sample exhibits square-shaped rods that are distributed irregularly. In other words, V_2O_5 nanorods can be seen scattered throughout the cotton-like SiO_2 framework and their distinct phases over a large area can be seen in Fig. 2b. TEM images provide crucial information about particle size, shape, and distribution. TEM imaging of Fig. 2c reveals that square plated nanorods of V_2O_5, along with the rGO–V_2O_5–SiO_2 framework, are present on the surface of the rGO nanosheets. However, the elongated direction of V_2O_5 flakes attached to the rGO nanosheets, as shown in Fig. 2d, creates a high wall surface in the 3-D architecture. This rough surface in the rGO–V_2O_5–SiO_2 composite facilitates rapid ion intercalation, leading to superior performance of the Pouch cell compared to using V_2O_5 alone. SEM images of a single sheet of rGO in Fig. S1 (ESI†) suggest its presence in the composite, and Fig. S2a and b (ESI†) shows a large area of V_2O_5 containing the nanospheres and SiO_2 all over the surface of the nanorods. EDS was employed to identify the composition of the rGO–V_2O_5–SiO_2 hybrid nanocomposite. The imaging spectra in Fig. S3 (ESI†) clearly show the dispersion of elements throughout the structure and confirm the presence of Si, V, C and O in the nanocomposite. According to quantitative elemental analysis in Fig. S2c (ESI†), the atomic ratio of Si/V is near the beginning proportion of the precursors.

XRD was used to describe the crystal structures of the rGO–V_2O_5–SiO_2 hybrid nanocomposite. Fig. 3a shows a broad peak in the SiO_2 XRD pattern, suggesting that the obtained SiO_2 is amorphous. No impurity peaks are visible in the V_2O_5 samples, and all peaks are compatible with orthorhombic V_2O_5 (JCPDS no. 41-1426). The two phases of V_2O_5 and SiO_2 are preserved after hydrothermal treatment, according to the XRD patterns of the V_2O_5–SiO_2 hybrid samples. After the addition of GO in the composite, according to the degree of reduction, the peak position of the GO sheets shifts into higher scattering angles when GO is reduced by thermal treatment and converting to rGO. The narrow and sharp diffraction peaks in the patterns indicate that the samples have a high degree of crystallinity. It is important to mention that the XRD peaks of the rGO–V_2O_5–SiO_2 hybrid nanocomposite are slightly shifted in comparison to V_2O_5, indicating that the partially reduced graphene nanosheets are evenly dispersed in the composites. This dispersion is facilitated by the presence of V_2O_5 nanoparticles resulting in increased interlayer spacing that may affect the crystal structure of the composite.[39]

Raman spectra have also been investigated to analyze the vibrational modes of the nanocomposite. There has been found a series of feature peaks at 98.03, 172.89, 272.52, 431.52, 509.16,

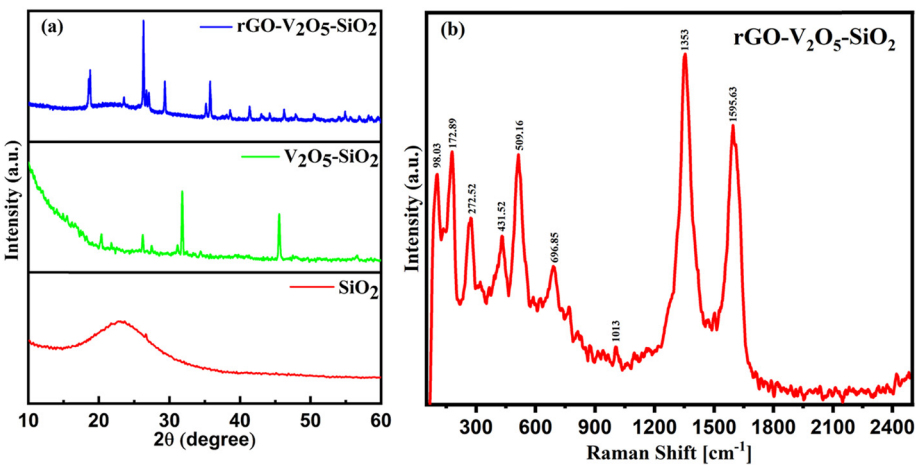

Fig. 3 (a) XRD spectra of rGO–V_2O_5–SiO_2, V_2O_5–SiO_2, and only SiO_2 materials; (b) Raman spectra of the composite (rGO–V_2O_5–SiO_2) under the irradiation of a 532 nm laser.

696.85, 1013, 1353, and 1595.63 cm^{-1} corresponding to vibration spectra of V_2O_5, SiO_2 and rGO. Under normal conditions, the lower wavenumber presented here as 98.03 and 172.89 cm^{-1} corresponds to the chain translational modes present in the layered structures, which shows a good agreement with the device intercalation mechanism. The significance of bending vibrations depicted by the peak at 272.52 and 431.52 cm^{-1} corresponds to V═O and V–O–V bonds, respectively. The Raman shift at 509.16 cm^{-1} can be connected to the stretching vibration of the V3–O bond by the oxygen with three coordinated V ions. Moreover, the Raman bands recorded at 1013 and 509.16 cm^{-1} correspond to the edge stretching vibration of the V1═O and V2–O bonds, respectively. Besides, the Raman shifts exhibited the intensities of the D and G peaks at 1364.2 and 1591.5 cm^{-1}, respectively in Fig. 3b.

The V_2O_5–SiO_2 and SiO_2 samples have been characterized by FT-IR spectroscopy (Fig. S4, ESI†), showing strong silica matrix bands. Both the materials display absorption peaks at 819, 1099, 1632, and 3473 cm^{-1}, corresponding to the vibration of doubly coordinated oxygen bonds (bridge oxygen), the stretching vibration of terminal oxygen bonds (V═O), the H–O–H bending, and the O–H stretching vibration modes of H_2O molecules, respectively. The bands at 798 cm^{-1} and 802 cm^{-1} are attributed to Si–O–Si symmetric stretching, while the broad bands in the 1000–1200 cm^{-1} range are attributed to asymmetric Si–O–Si stretching. Moreover, the broad bands observed at about 3400 cm^{-1} are attributed to O–H stretching vibration. SiO_2 framework vibrations dominate the FT-IR spectra of the V_2O_5–SiO_2 composite. However, the V═O stretching band at about 1010 cm^{-1} in the spectra might be attributed to asymmetric V–O–V stretching. The Raman spectrum has also been investigated to analyze the vibrational modes of the nanocomposite.

The electrochemical performance of the single pouch cell and its series combination is tested using a battery analyzer. As detailed in the experimental and supplementary information sections, the cathode material is prepared using the combination of rGO, SiO_2, and V_2O_5. The single pouch cell is fabricated in ambient conditions with the cathode material,

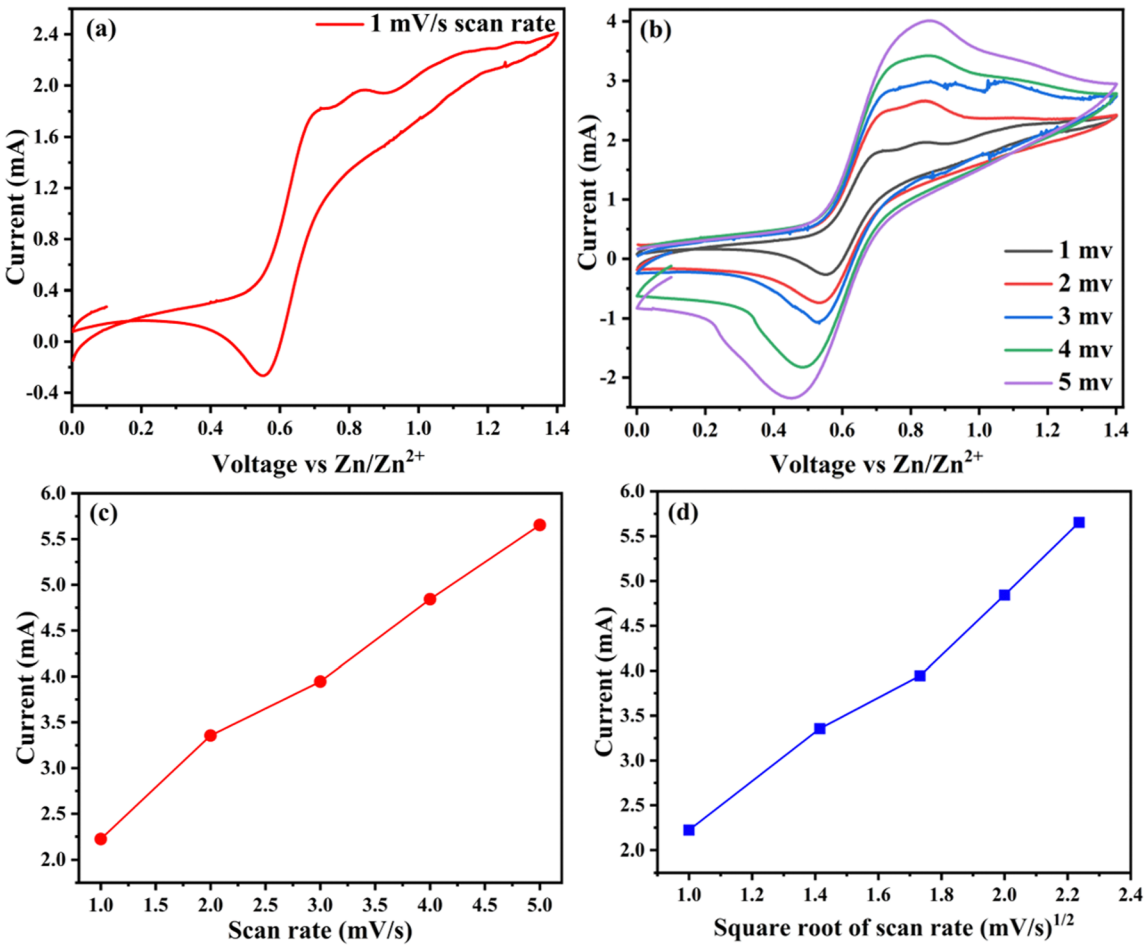

Fig. 4 (a) rGO–V_2O_5–SiO_2 cyclic voltammetry spectrum. We investigate the redox process of the rGO–V_2O_5–SiO_2 cathode to explain the high-rate performance. This picture depicts the cathode's cyclic voltammetry (CV) curves at a scan rate of 1.0 mV s^{-1}. The figure demonstrates two pairs of redox peaks in the CV curves that are compatible with the steady discharge charge profiles. (b) CV curves of rGO–V_2O_5–SiO_2 at different scan rates from 1.0 to 5.0 mV s^{-1}. Electrochemical fitting and theoretical calculation of the long-term chemical kinetics. (c and d) Fitting of the multi-sweep rate CV curves ranging from 1 to 5 mV s^{-1}.

i.e., the rGO–V_2O_5–SiO_2 nanocomposite, zinc foil as an anode, and Zn $(CF_3SO_3)_2$ as the aqueous electrolyte. Fig. 4a shows the CV of rGO–V_2O_5–SiO_2 at a scan rate of 1.0 mV s^{-1}. During the anodic scan run, two peaks are observed, one at 0.71 V and the other at 0.83 V, which shows the oxidation peaks, and the *vice versa* reduction peak are also observed at 0.54, which are caused by the zinc ion intercalation/deintercalation during the discharge/charge processes. This suggests that the zinc ions are involved in the electrochemical processes of the Zn/rGO–V_2O_5–SiO_2 electrodes with the hybrid Zn $(CF_3SO_3)_2$ electrolyte. An improvement has been recorded in the electrochemical performance as observed in the CV graphs, which may be the effect of the cotton-like structure of SiO_2 around V_2O_5 on the rGO planes, showing a good agreement with the SEM results. Fig. 4b displays reaction kinetics obtained through CV curves, demonstrating that the shapes of the curves remain well-maintained even with increasing scan rates. This indicates that the charge storage mechanisms in the Zn–rGO–V_2O_5–SiO_2 nanocomposite battery are robust and unaffected by changes in the scan rate. The well-maintained shapes of the CV curves imply that the charge storage processes within the nanocomposite are reversible and occur at a relatively fast rate. In addition to this, current *versus* scan rates and square root of scan rates as shown in Fig. 4c and d exhibit linear behaviour with increased scan rate.[40] The absence of significant changes in the curves with increasing scan rates suggests that the charge transfer kinetics are not limited by the surface adsorption rate, diffusion processes, or other factors that could cause deviations in the CV curves.[41] The consistent shape of the CV curves over a range of scan rates is often indicative of a highly conductive and stable electrode material. This suggests that the Zn–rGO–V_2O_5–SiO_2 nanocomposite possesses favourable properties for energy storage applications, such as efficient charge transfer and minimal degradation over multiple charge–discharge cycles.[42,43] The typical galvanostatic discharge/charge curves of the rGO–V_2O_5–SiO_2 hybrid nanocomposite in an aqueous electrolyte (0.5 M Zn $(CF_3SO_3)_2$) at a current density of 200 mA g^{-1} are shown in Fig. 5c. The initial discharge and charge capacity values of the rGO–V_2O_5–SiO_2 nanocomposite based on the weight of total cathode material was found to be 500 and 640 mA h g^{-1}, respectively. The V_2O_5 squared nanorods, covered with SiO_2, are dispersed on rGO as shown in the SEM and TEM, indicating that the surface of the V_2O_5 nanorods in contact with the electrolyte is increased, which might contribute to the exhibited higher capacity. Additionally, the mesoporous SiO_2 might facilitate mass transport during the charge/discharge process, increasing the capacity. Fig. 5a and b display the cycling performances of the hybrid nanocomposite rGO–V_2O_5–SiO_2 in

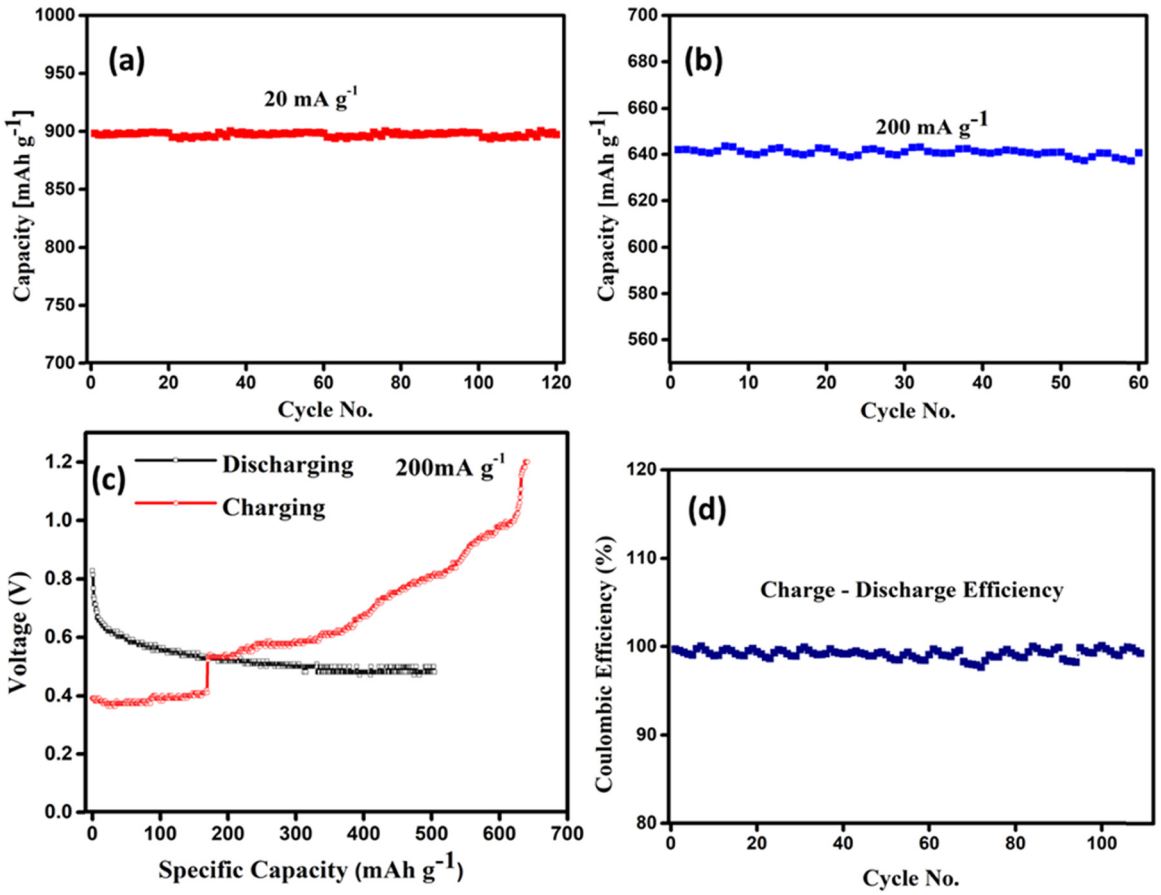

Fig. 5 Galvanostatic charge–discharge profiles at varying current densities. (a) Cycle performance at different current densities at 20 mA g^{-1} and (b) 200 mA g^{-1}; (c) voltage supply at different specific capacities; (d) coulombic efficiency of a single cell.

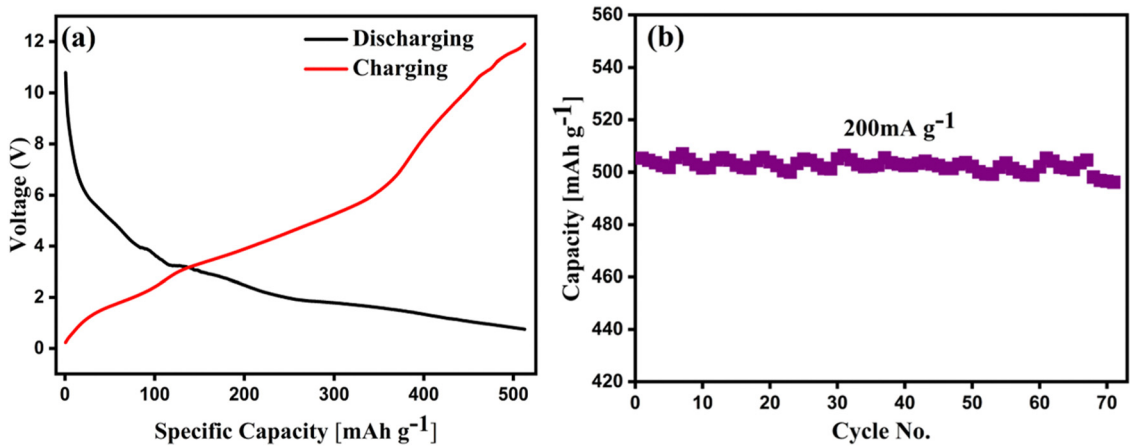

Fig. 6 (a) 12 V battery power supply at different specific capacities; (b) cycling performance of the 12 V battery at a constant current density of 200 mA g^{-1}.

an aqueous electrolyte. It was found in Fig. 5a that the capacities of rGO–V_2O_5–SiO_2 maintain the initial capacity of 890 mA h g^{-1} up to 120 cycles of charge/discharge in the aqueous electrolyte at a current density of 20 mA g^{-1}. The corresponding coulombic efficiencies around ~100 at 20 mA g^{-1} have been shown in Fig. 5d, which is in good agreement with the cyclic retention data of the cell. Similar behavior has been shown in Fig. 5b at a higher current density of 200 mA g^{-1}.

This consistency in the capacity values can be attributed to the significant reduction in the phase change of the active materials. The reaction occurs between the active material in the presence of adsorbed water of SiO_2 and without the disintegration of the electrolyte or the dissolution of transition metal ions. The following reactions show the cathodic and anodic process on the electrodes.

Electrochemical Impedance Spectroscopy (EIS) was employed to gain additional insights into the system. The Nyquist plot, along with its corresponding Bode plot, revealed a linear trend in the high-frequency region for the charged device at 1.4 V. This linear trend suggests the association and dissociation of Zn metal ions within the system in Fig. S6 (ESI†). Additionally, a closer examination of the Nyquist plots using the –equivalent circuit'' model indicated significant variability in the interfacial charge transfer resistance within the electrolyte. Table S1 (ESI†) shows the fitting factor with *R*1, *R*2, *P*2, and *n*1, which are the resultants of the fitting of the equivalent circuit.[40,44] The study indicates that the synergistic effect of the water adsorption capacity of SiO_2 and the structural capabilities of V_2O_5 play a significant role in high-capacity ZIBs. Also, the aqueous 0.5 M Zn $(CF_3SO_3)_2$ electrolyte supports better cycling stability by decreasing the water molecules surrounding Zn^{2+} ions, thus improving charge transfer.[45–47] In Fig. 6, the series combination of the individual cell produces 12 V energy. A total of 9 cells are connected in this configuration, as shown in Fig. S5 (ESI†). The corresponding charging–discharging performance of the cell stack is shown in Fig. 6a. The cycling performance of the 12 V battery configuration at the current density of 200 mA g^{-1} demonstrates a high specific capacity of >500 mA h g^{-1}, as shown in Fig. 6b. This pouch cell configuration is an attempt to realize the potential of the zinc ion battery for commercial applications. The parameters of the Zn ion battery are summarized and compared with other reported literature. Table S2 and Note 1 (ESI†) show a comparison of the coin cell and pouch cell capacities. Of note, the stability of the electrode is preserved even after a long cycling duration. It can be clearly seen in Fig. S7a and b (ESI†) that the Zn sheet is maintained with integrity of its structure. However, some of the parts look etched at the nanoscale, which could be attributed to the initial dissolution of zinc to achieve equilibrium with the Zn $(CF_3SO_3)_2$ electrolyte. On another hand, Fig. S7c and d (ESI†) clearly show the well preserved composite morphology after a long duration of 120 cycles. SiO_2 with a spherical cotton-like structure with V_2O_5 nanoplates and the presence of rGO sheets can be visualized from the FESEM micrographs. The EDS spectra for a square shaped area in Fig. S7e and f (ESI†) also depict the minimum dissolution of the zinc after 120 cycles, which was also reported earlier to demonstrate the chemical kinetics of the cell.[48]

3. Conclusions

In conclusion, we have developed a rGO–V_2O_5–SiO_2 nanocomposite-based cathode material in an aqueous electrolyte-driven ZIB using a hydrothermal technique. The synthesized material was analyzed using XRD graphs and FESEM demonstrating the existence of a porous structure in the cathode material, thus providing an enhanced interlayer spacing for Zn^{2+} intercalation. The resultant Zn–rGO–V_2O_5–SiO_2 cathode can deliver a high capacity of 890 mA h g^{-1} at 20 mA g^{-1} along with excellent rate performance and cycling stability (~97% capacity retention for at least 120 cycles). Extensive characterization of the cathode material at different charge/discharge states revealed that the cathode is highly reversible and stable.

Author contributions

All the authors took part in the discussion to understand the results and approved the final draft of the manuscript.

Conflicts of interest

The authors declare no competing financial interest.

Acknowledgements

The authors thank IIT Jammu and CSIR-CMERI for their valuable support. AL is thankful to MoE, GOI for the fellowship assistance. The authors are also grateful to DST-SERB, India for financial support under the Empowerment and Equity Opportunities for Excellence in Science (EMEQ) Scheme through research grant number (EEQ/2017/000220).

References

1 L. Zhou, Y. Wang, H. Jia, H. Gong, L. Liu and T. Du, *Sustainable Energy Fuels*, 2022, **6**, 1727–1732.
2 R. Raccichini, A. Varzi, S. Passerini and B. Scrosati, *Nat. Publ. Gr.*, 2014, **14**, 271–279.
3 G. Xiong, P. He, B. Huang, T. Chen, Z. Bo and S. Fisher, *Nano Energy*, 2017, **38**, 127–136.
4 Y. Huang, J. Mou, W. Liu, X. Wang and L. Dong, *Nano-Micro Lett.*, 2019, **11**, 1–13.
5 G. Fang, J. Zhou, A. Pan and S. Liang, *ACS Energy Lett.*, 2018, **3**, 2480–2501.
6 P. He, Z. Ding, X. Zhao, J. Liu, S. Yang, P. Gao and L. Fan, *Inorg. Chem.*, 2019, **58**, 12724–12732.
7 K. Liu, Y. Liu, D. Lin, A. Pei and Y. Cui, *Sci. Adv. Mater. Sci.*, 2018, **4**, 1–11.
8 J. M. Tarascon and M. Armand, *Nature*, 2001, **414**, 359–367.
9 F. Wan, Y. Zhang, L. Zhang, D. Liu, C. Wang, L. Song and Z. Niu, *Angew. Chem.*, 2019, **230026**, 7062–7067.
10 Z. Batteries, M. T. Nguyen, T. Yonezawa, J. Ma and S. Kheawhom, *Energies*, 2020, **13**, 1–13.
11 B. Tang, L. Shan, S. Liang and J. Zhou, *Energy Environ. Sci.*, 2019, **12**, 3288–3304.
12 M. Song, H. Tan, D. Chao and H. J. Fan, *Adv. Funct. Mater.*, 2018, **28**, 1–27.
13 H. Pan, Y. Shao, P. Yan, Y. Cheng, K. S. Han, Z. Nie, C. Wang, J. Yang, X. Li, P. Bhattacharya, K. T. Mueller and J. Liu, *Nat. Energy*, 2016, **1**, 1–7.
14 G. Kasiri, R. Trócoli, A. Bani Hashemi and F. La Mantia, *Electrochim. Acta*, 2016, **222**, 74–83.
15 T. Gupta, A. Kim, S. Phadke, S. Biswas, T. Luong, B. J. Hertzberg, M. Chamoun, K. Evans-Lutterodt and D. A. Steingart, *J. Power Sources*, 2016, **305**, 22–29.
16 H. Liang, Z. Cao, F. Ming, W. Zhang, D. H. Anjum and Y. Cui, *Nano Lett.*, 2019, **19**, 3199–3206.
17 Y. Cheng, L. Luo, L. Zhong, J. Chen, B. Li, W. Wang, S. X. Mao, C. Wang, V. L. Sprenkle, G. Li and J. Liu, *ACS Appl. Mater. Interfaces*, 2016, **8**, 13673–13677.
18 N. Zhang, Y. Dong, M. Jia, X. Bian, Y. Wang, M. Qiu, J. Xu, Y. Liu, L. Jiao and F. Cheng, *ACS Energy Lett.*, 2018, **3**, 1366–1372.
19 B. Sambandam, V. Soundharrajan, S. Kim, M. H. Alfaruqi, J. Jo, S. Kim and V. Mathew, *J. Mater. Chem. A*, 2018, **6**, 15530–15539.
20 D. Kundu, P. Oberholzer, C. Glaros, A. Bouzid, E. Tervoort, A. Pasquarello and M. Niederberger, *Chem. Mater.*, 2018, **30**, 3874–3881.
21 G. Dawut, Y. Lu, L. Miao and J. Chen, *Inorg. Chem. Front.*, 2018, **5**, 1391–1396.
22 G. Fang, S. Liang, Z. Chen, P. Cui, X. Zheng, A. Pan, B. Lu, X. Lu and J. Zhou, *Adv. Funct. Mater.*, 2019, **29**, 1–9.
23 M. Liao, J. Wang, L. Ye, H. Sun, Y. Wen, C. Wang, X. Sun, B. Wang and H. Peng, *Angew. Chem.*, 2020, **132**, 2293–2298.
24 Y. Zhang, J. Qin, M. Batmunkh, W. Li, H. Fu, L. Wang, M. Al-Mamun, D. Qi, P. Liu, S. Zhang and Y. L. Zhong, *Small*, 2022, **2105761**, 2105761.
25 F. Coustier, S. Passerini, J. Hill and W. H. Smyrl, *J. Electrochem. Soc.*, 1999, **146**, 1355–1360.
26 S. Zhang, H. Tan, X. Rui and Y. Yu, *Acc. Chem. Res.*, 2020, **53**, 1660–1671.
27 R. Chen, T. Zhao, J. Lu, F. Wu, L. Li, J. Chen and G. Tan, *Nanoletters*, 2013, **13**, 4642–4649.
28 Q. Pang, C. Sun, Y. Yu, K. Zhao, Z. Zhang, P. M. Voyles, G. Chen, Y. Wei and X. Wang, *Adv. Energy Mater.*, 2018, **8**, 1–9.
29 R. Sahoo, T. H. Lee, D. T. Pham, T. H. T. Luu and Y. H. Lee, *ACS Nano*, 2019, **13**, 10776–10786.
30 H. Huang, X. Wang, E. Tervoort, G. Zeng, T. Liu, X. Chen, A. Sologubenko and M. Niederberger, *ACS Nano*, 2018, **12**, 2753–2763.
31 K. Palanisamy, J. H. Um, M. Jeong and W. S. Yoon, *Sci. Rep.*, 2016, **6**, 1–12.
32 P. Xue, C. Guo, N. Wang, K. Zhu, S. Jing, S. Kong, X. Zhang, L. Li, H. Li, Y. Feng, W. Gong and Q. Li, *Adv. Funct. Mater.*, 2021, **31**, 1–10.
33 J. Huang, Y. Li, R. Xie, J. Li, Z. Tian, G. Chai, Y. Zhang, F. Lai, G. He, C. Liu, T. Liu and D. J. L. Brett, *J. Energy Chem.*, 2021, **58**, 147–155.
34 Z. Zhang, H. Wang, S. Ji, B. G. Pollet and R. Wang, *Ionics*, 2016, **22**, 1593–1601.
35 S. Wang, K. Zhu, L. Yang, H. Li, S. Wang, S. Tang and M. Zhang, *Ionics*, 2020, **26**, 5607–5615.
36 G. Du, H. Seng, Z. Guo, J. Liu, W. Li, D. Jia and C. Cook, *RSC Adv.*, 2011, 690–697.
37 S. Gupta, B. Aberg, S. B. Carrizosa and N. Dimakis, *Materials*, 2016, **9**(8), 615.
38 W. Gou, H. Chen, Z. Xu, Y. Sun, X. Han, M. Liu and Y. Zhang, *Energy Adv.*, 2022, **1**, 1065–1070.
39 T. N. Vinuth Raj, P. A. Hoskeri, S. Hamzad, M. S. Anantha, C. M. Joseph, H. B. Muralidhara, K. Yogesh Kumar, F. A. Alharti, B. H. Jeon and M. S. Raghu, *Inorg. Chem. Commun.*, 2022, **142**, 109648.
40 S. Zhu, Y. Dai, J. Li, C. Ye, W. Zhou, R. Yu, X. Liao, J. Li, W. Zhang, W. Zong, R. Chen, G. He, D. Chao and Q. An, *Sci. Bull.*, 2022, **67**, 1882–1889.
41 M. Narayanasamy, B. Kirubasankar, M. Shi, S. Velayutham, B. Wang, S. Angaiah and C. Yan, *Chem. Commun.*, 2020, **56**, 6412–6415.
42 L. Zhang, M. Zhang, H. Guo, Z. Tian, L. Ge, G. He, J. Huang, J. Wang, T. Liu, I. P. Parkin and F. Lai, *Adv. Sci.*, 2022, **9**, 1–10.

43 W. Zong, H. Guo, Y. Ouyang, L. Mo, C. Zhou, G. Chao, J. Hofkens, Y. Xu, W. Wang, Y. E. Miao, G. He, I. P. Parkin, F. Lai and T. Liu, *Adv. Funct. Mater.*, 2022, **32**, 2110016.
44 Y. Dai, C. Zhang, W. Zhang, L. Cui, C. Ye, X. Hong, J. Li, R. Chen, W. Zong, X. Gao, J. Zhu, P. Jiang, Q. An, D. J. L. Brett, I. P. Parkin, G. He and L. Mai, *Angew. Chem., Int. Ed.*, 2023, **62**, 1–7.
45 D. Bin, W. Huo, Y. Yuan, J. Huang, Y. Liu, Y. Zhang, F. Dong, Y. Wang and Y. Xia, *Chem*, 2020, **6**, 968–984.
46 P. Sehrawat, A. Abid, S. S. Islam and A. Mauger, *C*, 2020, **6**(4), 81.
47 N. Zhang, Y. Dong, M. Jia, X. Bian, Y. Wang, M. Qiu, J. Xu, Y. Liu, L. Jiao and F. Cheng, *ACS Energy Lett.*, 2018, **3**(6), 1366–1372.
48 W. Li, K. Wang, S. Cheng and K. Jiang, *Energy Storage Mater.*, 2018, **15**, 14–21.